

## Full length article

# On the origin of creep dislocations in a Ni-base, single-crystal superalloy: an ECCI, EBSD, and dislocation dynamics-based study



Farangis Ram <sup>a,\*</sup>, Zhuangming Li <sup>a</sup>, Stefan Zaefferer <sup>a</sup>, Seyed Masood Hafez Haghghat <sup>a</sup>, Zailing Zhu <sup>b</sup>, Dierk Raabe <sup>a</sup>, Roger C. Reed <sup>b</sup>

<sup>a</sup> Max-Planck Institut für Eisenforschung GmbH, Max-Planck-str. 1, 40237, Düsseldorf, Germany

<sup>b</sup> Department of Materials, University of Oxford, Parks Road, Oxford OX1 3PH, UK

## ARTICLE INFO

## Article history:

Received 29 August 2015

Received in revised form

13 February 2016

Accepted 18 February 2016

Available online xxx

## Keywords:

Single-crystal, Ni-base superalloys

Creep dislocations

Dislocation dynamics

Low-angle grain boundaries

## ABSTRACT

This work investigates the origin of creep dislocations in a Ni-base, single crystal superalloy subject to creep at an intermediate stress and temperature. Employing high angular resolution electron backscatter diffraction (HR-EBSD), electron channeling contrast imaging under controlled diffraction conditions (cECCI) and discrete dislocation dynamics (DDD) modelling, it is shown that low-angle boundaries—which correspond to dendrite boundaries or their residues after annealing—are not the major sources of creep dislocations. At the onset of creep deformation, they are the only active sources. Creep dislocations are emitted from them and percolate into the dislocation-depleted crystal. However, the percolation is very slow. As creep deformation proceeds, before the boundary-originated dislocations move further than a few micrometers away from their source boundary, individual dislocations that are spread throughout the undeformed microstructure become active and emit avalanches of creep dislocations in boundary-free regions, i.e. regions farther than a few micrometer away from boundaries. Upon their activation, the density of creep dislocations in boundary-free regions soars by two orders of magnitude; and the entire microstructure becomes deluged with creep dislocations. The total area of boundary-free regions is several times the total area of regions covered by boundary-originated creep dislocations. Therefore, the main sources of creep dislocations are not low-angle boundaries but individual, isolated dislocations in boundary-free regions.

© 2016 Acta Materialia Inc. Published by Elsevier Ltd. All rights reserved.

## 1. Introduction

Nickel-base superalloys are employed in high-temperature applications, particularly for jet propulsion and power conversion. To increase creep resistance, these alloys are produced as single crystals. Single-crystal superalloys are often fabricated by directional solidification techniques using competitive dendrite growth [1,2]. Casting is usually followed by a solution and ageing heat-treatment to achieve the desired microstructure [3,4] consisting of about 70% volume fraction of cuboidal  $\gamma'$  precipitates coherently embedded in a solid solution  $\gamma$  matrix.

The as-processed  $\gamma/\gamma'$  microstructure is dislocation-depleted. As creep-deformation proceeds, the microstructure becomes increasingly populated with creep dislocations [5–10]. In tertiary creep

regime, characterized by a monotonically increasing strain rate, it has been suggested that sources of creep dislocations are the so-called grown-in networks of dislocations [11–14]. These networks, which are casting defects and which withstand the subsequent heat-treatment, are in fact low-angle grain boundaries.

It has been shown that the as-processed single crystals are not truly monocrystalline: low-angle boundaries exist, which accommodate lattice rotations of below  $1^\circ$  [15–19]. Instances of dislocation percolation from a boundary to dislocation-depleted crystal portions in the close vicinity of the grown-in low angle grain boundaries—a few micrometers—have been observed in TEM foils [11–14]. It has been suggested that: the boundary-generated dislocation loop segments are driven into the narrow  $\gamma$  channels by a shear stress, which results from the superposition of the applied stress and the misfit stress; during glide in the  $\gamma$  channels, the permeating dislocations deposit segments at the  $\gamma/\gamma'$  interfaces [4]; these dislocations partially relieve the  $\gamma/\gamma'$  misfit stress; and the gliding dislocations originated from different boundaries

\* Corresponding author. Materials Science and Engineering Department, Carnegie Mellon University, 5000 Forbes Avenue, Pittsburgh, 15213-3890, PA, USA.  
E-mail address: [fram@cmu.edu](mailto:fram@cmu.edu) (F. Ram).

eventually meet, react, and result in dislocation networks [11,13,20].

The research reported in this paper was carried out to revisit the sources of creep dislocations by examining the evolution of dislocation density throughout the microstructure. A Re-containing Ni-base, single-crystal superalloy was studied to elucidate the microstructural evolution that control the early stages of creep deformation. Electron channeling contrast imaging (ECCI) and electron backscatter diffraction (EBSD) techniques were employed for microstructure characterization; and discrete dislocation dynamics (DDD) modelling was utilized for simulating the microstructural evolutions.

## 2. Materials and methods

The single-crystal superalloy studied here was prepared in the form of cylindrical bars of 10 mm diameter and 160 mm length using investment casting. Its chemical composition, Ni–8Cr–10Co–1.6Re–8.5W–5.8Al–8.5Ta in weight percent, was chosen consistent with the alloy design results of [21]. An industrial-scale investment casting facility was used for casting with a withdrawal speed of 229 mm/h, a mould temperature of 1540 °C and a vacuum of better than  $10^{-4}$  Pa. After casting, the single-crystal bars were carefully removed from the mould, sand blasted, macro-etched using an HCl + 5–10 vol.% H<sub>2</sub>O<sub>2</sub> solution, and subjected to X-ray analysis using the back-reflection Laue technique to confirm their <001> orientation. Solution treatment was then carried out at 1305 °C for 6 h followed by a two-step heat-treatment at 1120 °C for 3 h and at 870 °C for 16 h. Tensile testpieces of 20 mm gauge length and 4 mm diameter were then machined from the fully heat-treated single-crystal bars such that their long axes were parallel to the growth direction of the single crystal, which is a <001> crystallographic direction. A schematic is shown in Fig. 1 a.

The tensile testpieces were subsequently subjected to a constant-load creep test at 900 °C up to rupture. Within the gauge section, the applied stress was uniaxial tensile of 450 MPa. The creep curve, displayed in Fig. 1 b, indicates a tertiary creep regime identified by the monotonic increase of strain rate with strain [4]. Rupture occurred at 22.1% strain after 194 h. The investigations reported in this paper were performed on the ruptured testpiece and were confined to a region of the testpiece close to the extensometer lips, where the accumulated local strain was estimated to be less than 0.1%.

The microstructure was examined using ECCI [22–24] and EBSD [25] in a Scanning Electron Microscope (SEM). ECCI was performed using a Zeiss Merlin scanning electron microscope (Carl Zeiss SMT AG, Germany) with a Gemini-type field emission gun electron column. The microscope was operated at 30 kV accelerating voltage and 2–5 nA probe current. The specimen was placed at 6 mm working distance and was tilted to an angle in the range  $[-4^{\circ}, 20^{\circ}]$ . To observe dislocations, the ECCI under controlled diffraction conditions (cECCI) method [23] was employed. The computer program TOCA [26,27] was used for selection of suitable diffraction conditions from simulated electron channeling pattern (ECP).

EBSD measurements were carried out in a JEOL 6500F FEG scanning electron microscope operating at 15 kV accelerating voltage and high beam current mode and equipped with a Digiview 5 camera and the EDAX/TSL OIM DC software (version 7.0; EDAX/TSL, Draper, UT, USA). Patterns were captured with  $2 \times 2$  binning on the camera, minimum camera gain, no averaging, no background removal, and no image processing. The recorded patterns were of  $468 \times 468$  dimensionality with 12 bit depth. Beam scanning was performed in 1  $\mu\text{m}$  or 2  $\mu\text{m}$  steps.

Crystal orientation maps were measured using the EDAX/TSL

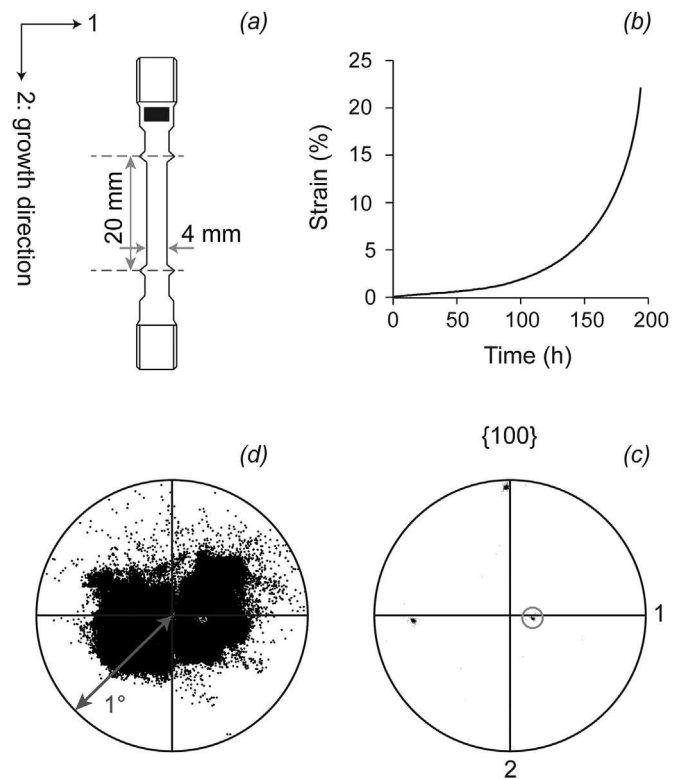


**Fig. 1.** (a) Schematic illustration of the examined testpiece before the creep test. The black rectangle marks the region that contains the EBSD-mapped areas. (b) The creep curve showing the engineering strain versus time at 900 °C and 450 MPa. (c) EBSD-based {100}-pole figure in stereographic projection of a region in the uncrept area. (d) The pole circled in (c) is magnified by rotating it to the center of the pole figure and setting the maximum polar angle to 1°.

OIM DC software. The Kikuchi bands utilized for orientation derivation were detected using the classical two-dimensional Hough transform (2-D HT)-based algorithm [28,29]. Patterns were binned to  $468 \times 468$  prior to applying the 2-D HT;  $160 \times 160$  was set for Hough space resolution; a  $\Delta\theta = 0.5^{\circ}$  pixels convolution mask was applied; and maximum 12 Kikuchi bands were used for orientation derivation.

Crystal rotations relative to a reference point on the map were obtained by applying the HR-EBSD method [30,31]. The density of geometrically necessary dislocations (GND) was computed using the HR-EBSD-based lattice curvature [32–34]. With a cubic symmetry, the three elastic stiffness constants at room temperature were assumed to be equal to the ones of CMSX-4, i.e.  $13 \times 13$  MPa;  $C_{11} = 243$  MPa; and  $C_{12} = 153$  MPa [35]. The CrossCourt software v.3 (BLG Productions Ltd., UK) was used for lattice rotation and GND density calculations [30,32,36]. On each pattern, 28 regions of interests each of  $C_{44} = 128$  pixels were considered.

To assess the evolution of dislocations during creep deformation, discrete dislocation dynamics (DDD) modelling was employed. DDD is well suited for the simulation of creep effects associated with dislocation mobility and their interactions based on the elasticity theory of dislocations [37–43]. For this study, the ParaDiS code was used [44]. A hybrid dislocation mobility rule with a climb/glide mobility ratio of 0.1 [38] was used to mimic climb-assisted mobility of dislocations along the  $\gamma/\gamma'$  interfaces at high temperature, i.e.  $\sim 900$  °C. Isotropic elasticity with a shear modulus of 37 GPa and a Poisson ratio of 0.37 was assumed. The lattice parameter for the Ni alloy in the  $\gamma$  channels was taken as  $a = 0.36$  nm, which leads to a <110> Burgers vector length of

$|\mathbf{b}| = 0.25$  nm. More details on the simulation methodology are given in Ref. [38].

### 3. Results

#### 3.1. The uncrept state

The region of the ruptured testpiece marked by a black rectangle in Fig. 1 a was considered to be uncrept or undeformed here and was measured by EBSD. Later, in §3.2, it will be confirmed that it is truly undeformed. It must be noted that this region differs from the material before the creep test in that it is further heat-treated at the creep test temperature (900 °C) for the rupture life of the testpiece (194 h). The largest area measured by EBSD extended across 2 mm × 1 mm. The longer edge was parallel to the growth direction, which was a  $\langle 001 \rangle$  crystal direction and was coincident with the tensile axis. The step size was 2  $\mu\text{m}$ . Fig. 1 e shows the  $\{100\}$ -pole figure of this region obtained through the classical 2-D HT-based EBSD analysis. It must be noted that the longitudinal section measured by EBSD is parallel to the growth direction; however, the sample surface is not a  $\{100\}$ -plane; as visible in Fig. 1 c, the surface normal is 20° rotated away from a  $\langle 100 \rangle$  direction about the tensile axis. As evident from the pole figure in Fig. 1 d, which shows the encircled  $\{001\}$ -pole magnified, there is an orientation dispersion of about 1° in the measured area.

The orientation dispersion is due to a mosaicity, i.e. the presence of sub-grains, created by the competitive growth of closely oriented dendrites during solidification. This mosaicity is apparent in the backscattered electron (BSE) micrographs. Low-magnification BSE micrographs (Fig. 2 a and b) show the dendritic structures of the material. The mosaic structure in these micrographs, however, is overshadowed by the strong contrast caused by the chemical composition difference between a dendrite core and its perimeter: the heavy-element-depleted interdendritic region appears darker compared to the heavy-element-enriched dendrite core [4,17,45]. The mosaicity is better visible in BSE micrographs with higher magnifications, e.g. Fig. 2 c and d; and it is most apparent in interdendritic regions.

Due to the inability of the classical EBSD-based analysis in quantifying lattice rotations below 1° [46,47], HR-EBSD analysis was performed on the EBSD data. The HR-EBSD-based relative lattice rotation maps, kernel average misorientation (KAM) map, and GND map of a representative undeformed region are depicted in Fig. 3. Similar maps of other undeformed areas inside the black rectangle in Fig. 1 a are presented as supplementary material S1. The latter maps were measured with a 1  $\mu\text{m}$  step size.

On a relative lattice rotation map, the values  $\omega_{12}$ ,  $\omega_{23}$ , and  $\omega_{31}$  assigned to each point denote the angle of misorientation between that point and a pre-selected arbitrary point on the map about the sample coordinate axes 3, 1, and 2, respectively. The KAM-value can be interpreted as the mean misorientation of a point with respect to its nearest neighboring points on the map [48].

The results show that: (1) relative rotations occur about all three axes, and all three are of the same extent (Fig. 3 a–c); (2) the local lattice rotation remains below 0.5° (Fig. 3 d); (3) these rotations are not spatially random fluctuations; there is an intricate network of low-angle boundaries (Fig. 3 d); and (4) the density of the GNDs on the boundaries does not exceed  $5 \times 10^{13} \text{ m}^{-2}$  (Fig. 3 d). This is true for maps with a 2  $\mu\text{m}$  step size as well as maps with a 1  $\mu\text{m}$  step size. The reported GND density is given as the number of dislocations piercing through a unit area between two adjacent pixels. For every pixel of the map, it is calculated using the lattice curvature at that pixel.

As seen in Fig. 3 d, the elevated GND density across a low-angle boundary is not limited to one pixel. This indicates that the

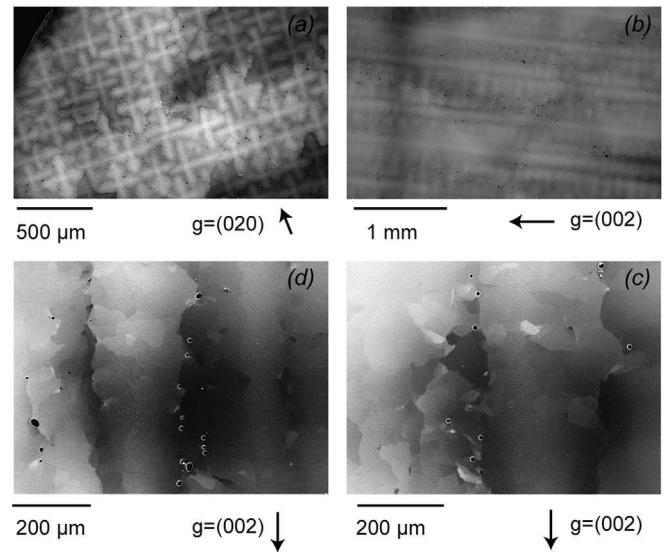


**Fig. 2.** Backscatter electron (BSE) micrographs of the uncrept region of the ruptured testpiece.—On the transverse section in (a) and the longitudinal section in (b), the dendritic structure is apparent. The black lines spanning over the micrographs in (a) and (b) correspond to channeling lines caused by the large sweeping angle of the electron beam over the single crystal area (Electron Channeling Pattern). The mosaicity is best visible in the magnified micrographs in (c) and (d).

boundaries are not sharp planar surfaces but wider regions. This is exemplified by the boundary displayed in Fig. 4. Fig. 4 a and b respectively show the KAM/GND density map and the ECC image of this boundary. The EBSD step size in Fig. 4 a is 1  $\mu\text{m}$ . Fig. 4 c shows the details of the part of the boundary that is enclosed by the green rectangle in Fig. 4 a and b. It shows that the boundary is not one pixel but several pixels wide. The maximum GND density on this boundary segment is  $\sim 4 \times 10^{13} \text{ m}^{-2}$ . Fig. 4 d shows the detailed dislocation structure of this boundary. It is clear that this dislocation structure is not the result of the intersection of a sharp boundary plane with the specimen surface; the boundary-surface intersection is rather spread over a few micrometers.

The most evident dislocation network of this boundary is encircled by a white ellipse in Fig. 4 d. Further to the left, several networks follow each adding its own misorientation and related dislocation density. The misorientation created by the encircled dislocation network can be estimated as follows. Fig. 5 shows a crystal, colored blue, embedded in a larger, transparent crystal. There is a misorientation between the two crystals with the angle  $\omega$ . The character of the boundary and the type of the dislocations that accommodate this misorientation varies with the orientation of the boundary plane. The boundary with the minimum number of dislocations is a pure tilt boundary (boundary 1 and 2), which is only composed of edge dislocations. For a pure tilt boundary, misorientation is obtained through  $\omega = |\mathbf{b}|/D$ , where  $D$  indicates the distance between dislocation lines, and  $\mathbf{b}$  is the Burgers vector of the dislocations. As evident from the schematic in Fig. 5, a twist boundary (boundary 3) requires a double number of dislocations to accommodate the same misorientation— $\omega = |\mathbf{b}|/(2D)$ . The number of dislocations in a mixed boundary (boundary 4) is between the number of dislocations in a tilt boundary and the number of dislocations in a twist boundary. The encircled boundary in Fig. 4 d is composed of a network of dislocations; therefore, it can be considered as a mixed boundary. The average spacing between the dislocations of this boundary is 30 nm. This is obtained by considering the dislocations that pierce through the specimen surface. For a  $1/2\langle 110 \rangle$  dislocation in nickel with  $|\mathbf{b}| = 0.25$  nm and

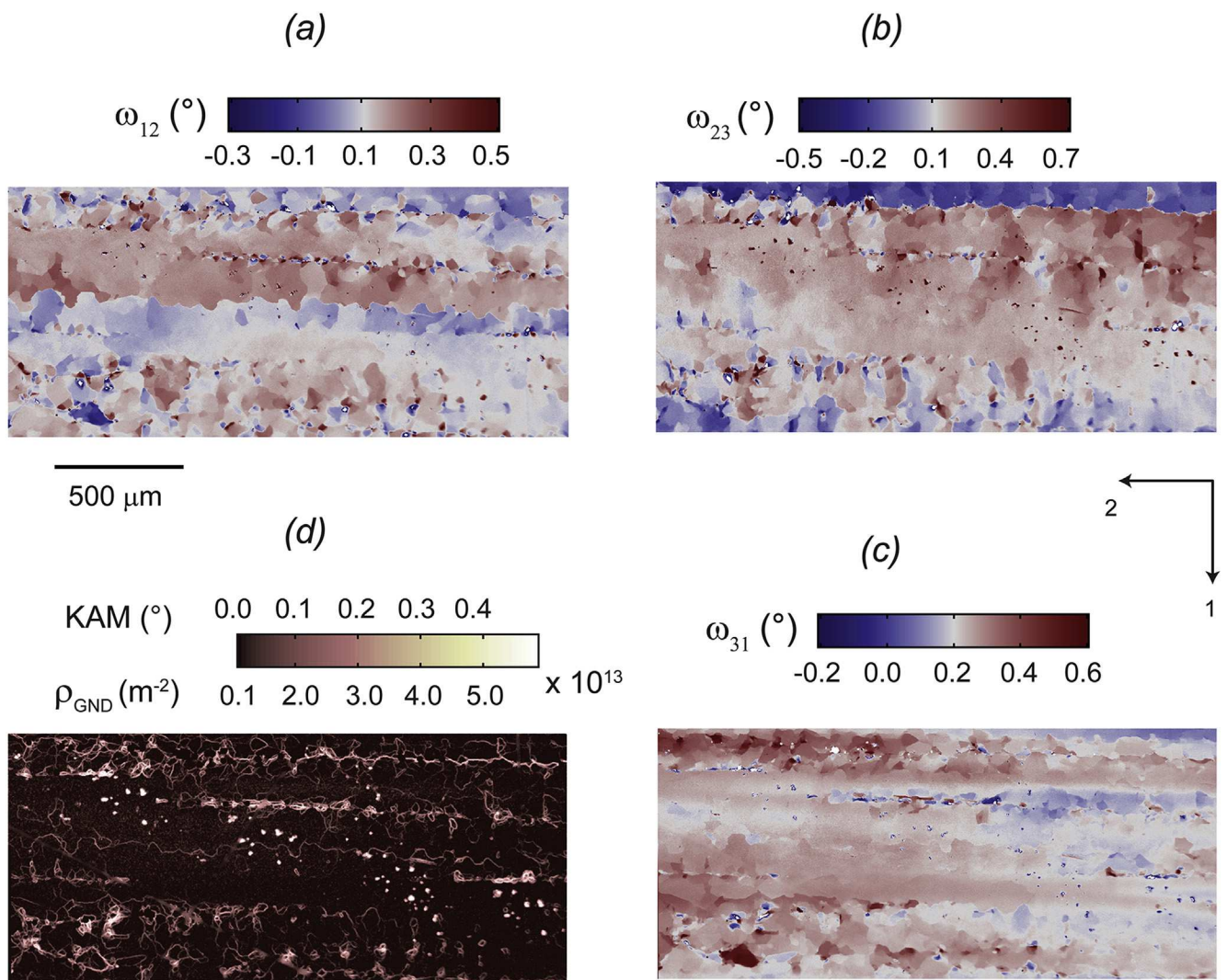


**Fig. 3.** HR-EBSD maps of a few dendrites in the undeformed region of the ruptured testpiece.—(a–c)  $\omega_{12}$ ,  $\omega_{23}$  and  $\omega_{31}$  are rotation angles about axes 3, 1, and 2, respectively. Rotations are relative to a point located at top right corner of the maps. (d) Kernel average misorientation (KAM) and geometrically necessary dislocation (GND) density map. Axis 2 is almost parallel to the growth direction. The scan step size is 2  $\mu\text{m}$ .

$D = 30 \text{ nm}$ , a tilt boundary's misorientation angle amounts to  $0.46^\circ$ , and a twist boundary's misorientation angle equates to  $0.23^\circ$ . Therefore, the misorientation angle of this boundary is between  $0.23^\circ$  and  $0.46^\circ$ . This misorientation angle is in good agreement with the misorientation angle obtained by HR-EBSD:  $\text{KAM} = 0.3^\circ$ .

It should be mentioned that the good agreement between the results of HR-EBSD and ECCI is due to the fact that all the dislocation networks in the spread-out boundary rotate the crystal in the same sense. Therefore, the EBSD measurements do not miss any orientation changes when stepping over the grain boundary area; and there is, consequently, no dependency of the EBSD-based GND density on the EBSD step size. For microstructures where the GND density depends on the EBSD step size [49,50], are to be consulted.

The spacing of the low-angle boundaries in the uncrept material is 30–150  $\mu\text{m}$  as the histogram in Fig. 6 shows. Each data point of this histogram was obtained by a line intercept method as follows. A straight line parallel to the shorter edge of the KAM map in Fig. 3 d was drawn; the points at which the line intersects a low-angle boundary were counted; and the length of the line was divided by the number of the intersection points. A total of 63 straight lines

were measured.

The ruptured testpiece is displayed in Fig. 7 a. The ECC micrographs of the typical microstructures found in the undeformed part of the testpiece (named A in Fig. 7 a) are displayed in Fig. 8 A1–A3. There are: (1) low-angle boundaries, which could be sharp planes, composed of one layer of dislocations (Fig. 8 A1) or a few micrometers wide (Fig. 8 A2 and Fig. 4 d)—the latter composing the majority of the boundaries; and (2) regions away from interdendritic boundaries, where in a few hundred square micrometers only a few isolated dislocations are present (Fig. 8 A3).

The results of the cECCI-based characterization of 155 dislocations on 27 randomly selected low-angle boundaries is presented in Table 1. It shows that 94% of dislocations have a  $\frac{1}{2}\langle 011 \rangle$  Burgers vector and 22% of total dislocations are sessile. The only non  $\frac{1}{2}\langle 011 \rangle$  dislocations have a  $\langle 100 \rangle$  Burgers vector and an edge character; hence, they are all sessile [51]. There are no dislocations in  $\gamma'$  precipitates. The characterization was performed using tilt experiments for trace line and Burgers vector analysis [23,24]. Please see supplementary material S2 for an example of such characterization.

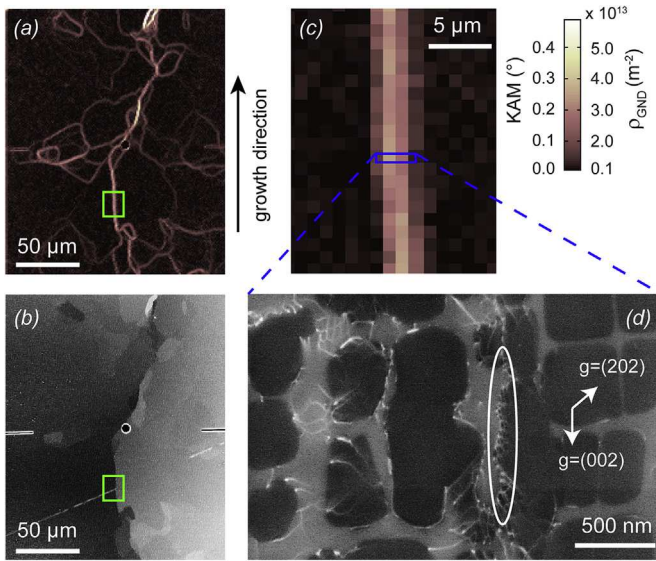


**Fig. 4.** Correlative investigations of the undeformed region of the ruptured testpiece by (a) HR-EBSD and (b) ECCI. The area inside the green rectangle in (a) and (b) is magnified in (c). ECC image of the part of the boundary enclosed by the blue rectangle in (c) is shown in (d). The oval in (d) encloses the part of the low-angle boundary, on which the dislocation density is highest. The step size of the EBSD map is 1 μm. (For interpretation of the references to colour in this figure legend, the reader is referred to the web version of this article.)

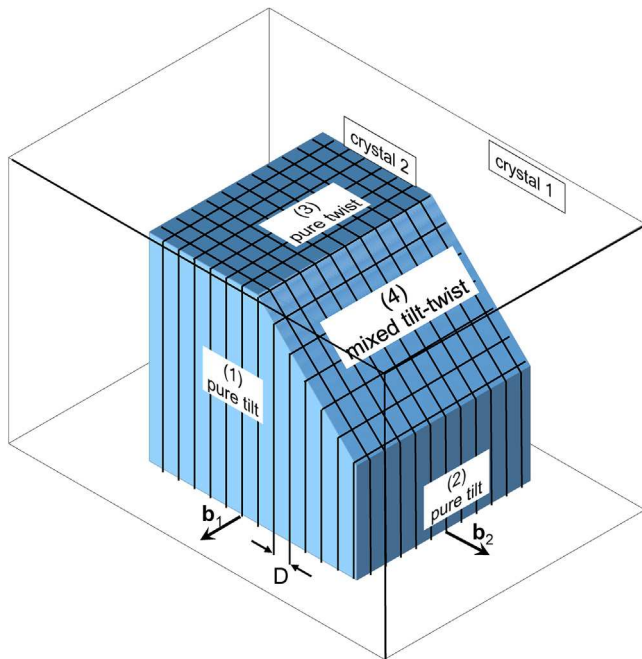


**Fig. 5.** A model for the accommodation of a misorientation by boundaries with different characters. The blue crystal is fully contained in the transparent crystal. They have a small misorientation of magnitude  $\omega$ . Depending on the orientation of the interface separating the two crystals, their misorientation is accommodated by networks of various mixtures of edge or screw dislocations; thus, creating boundaries of pure tilt, pure twist or any kind of mixed character. (For interpretation of the references to colour in this figure legend, the reader is referred to the web version of this article.)

### 3.2. The lightly-crept state

As this work is concerned with the source of creep dislocations, it is focused on the region of the ruptured testpiece that has

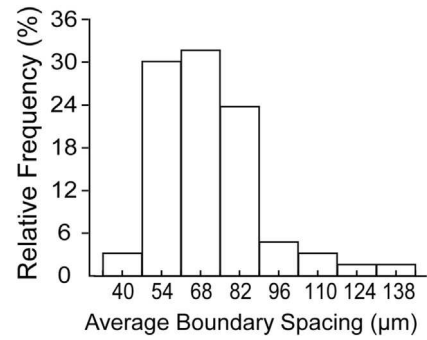


**Fig. 6.** The histogram of Low-angle boundary spacing in the undeformed region of the ruptured testpiece.

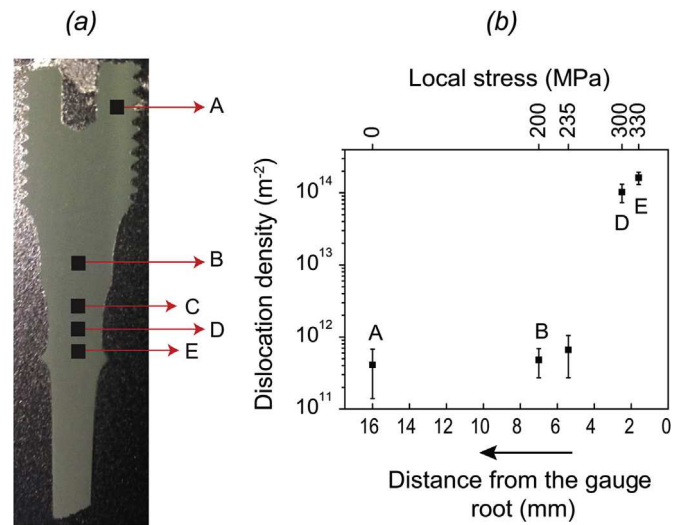


**Fig. 7.** (a) The ruptured testpiece.—Over sections marked as A–E, significant microstructural evolution take place. In (b), the average dislocation density away from low-angle boundaries is plotted for these sections. The local stress at each observed section is also plotted. Note that the local stress axis is not linearly scaled.

undergone less than 0.1% local strain. In Fig. 7 a, it is outside the gauge section before the gauge root. Although the strain level in this region is known to remain below 0.1%, the local strain value is unknown because this part of the testpiece was beyond the field of view of our strain measurement cameras. ECCI investigations on this lightly-crept region were performed on transverse sections normal to the tensile axis, and on longitudinal sections parallel to the tensile axis, which were either parallel to a {100} crystallographic plane or 20° rotated with respect to a {100} crystallographic plane.

Among the examined sections, those over which significant microstructural evolution take place are marked as A–E in Fig. 7 a. At section A (Fig. 7 a), which is located within grips, the applied tensile stress is assumed to be zero. At sections B–D, it is estimated by measuring the cross-sectional area: 128 × 128 MPa;  $\sigma(B) = 200$  MPa;  $\sigma(C) = 265$  MPa;  $\sigma(D) = 300$  MPa; and  $\sigma(D) = 330$  MPa. By comparing the microstructure of these sections, in effect, the evolution of the microstructure with the increment of applied tensile stress at a constant temperature (900 °C) and after a constant creep period (194 h) is being investigated.

ECCI results (Fig. 8) show that as the stress level increases, the dislocation structure varies. In the uncrept region (section A in Fig. 7 a), dislocations are concentrated at low-angle boundaries (Fig. 8 A1 and A2). Anywhere else, the microstructure is dislocation-

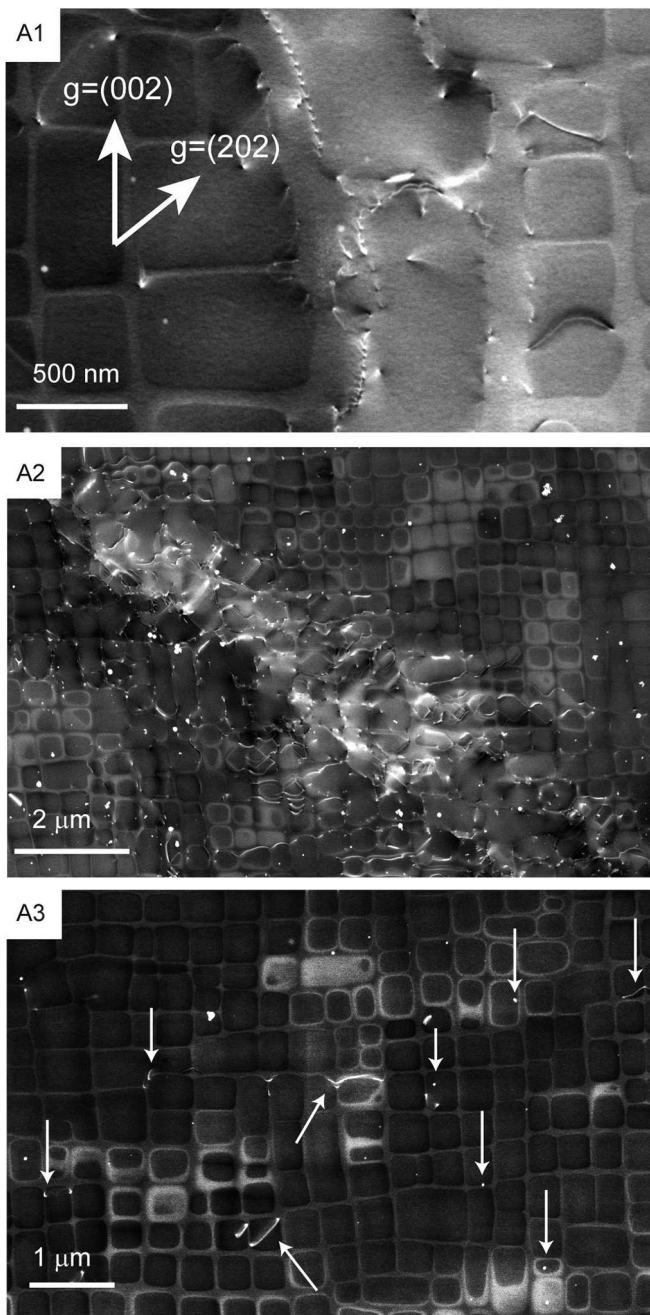


**Fig. 8.** cECCI micrographs of the dislocation structure of longitudinal and transverse sections (TS) at regions marked as A, B, C, and E in Fig. 7 a. All imaged surfaces are parallel to a {100} crystallographic plane. A “-TS” in a figure label marks a section perpendicular to the tensile axis. The remaining images are captured on longitudinal sections. The reflectors used for all depicted longitudinal and transverse sections are drawn in A1 and B4-TS respectively.

depleted—in areas of a few hundred square micrometers, there are only a few isolated dislocations (Fig. 8 A3). The average dislocation density away from the boundaries is  $5 \times 10^{11} \text{ m}^{-2}$  as the graph in Fig. 7 b shows. Each data point in this graph is obtained by counting the number of dislocations in more than 25 cECC micrographs of minimum  $10 \times 10 \mu\text{m}^2$  area. The measured regions were at least  $40 \mu\text{m}$  away from the inherited grown-in low-angle boundaries. The dislocation density was measured as “dislocation intersections per surface area” rather than “dislocation length per volume”. The latter definition results in about 2 times higher values, provided

that the dislocation lines are randomly distributed [52].

At section B (Fig. 7 a), where the applied stress is about 200 MPa, there are regions where dislocations are found only at low-angle boundaries. There are also regions in the vicinity of the low-angle boundaries—extending to a maximum of  $5 \mu\text{m}$  away from the boundary—that contain a noticeable dislocation content (Fig. 8 B1-TS and B2). The latter compose almost 10% of the microstructure in section B. In such regions, there is evidence for the emission of dislocations from the boundary into the undeformed crystal—e.g. dislocation loop segments marked in Fig. 8 B1-TS and B2, which have percolated through the adjoining dislocation-depleted crystal and left segments at several contiguous  $\gamma/\gamma'$  interfaces (also see e.g. Ref. [14]). A magnified percolating dislocation loop segment in a longitudinal section parallel to a {100} crystallographic plane is displayed in Fig. 8 B3. The boundary-originated dislocation loop segments are in horizontal channels giving evidence of a negative lattice misfit [4,13]. The remaining microstructure is dislocation-depleted (Fig. 8 B4-TS). The average dislocation density away from boundaries in section B does not change compared to section A: it is  $5 \times 10^{11} \text{ m}^{-2}$  (Fig. 7 b).

At section C, regions with a high density of dislocations appear both in the vicinity of boundaries (Fig. 8 C1) and away from the boundaries (Fig. 8 C2). In these regions, all  $\gamma/\gamma'$  interfaces are uniformly avalanched with dislocations. In some of these regions, rafting—i.e. the directional coalescence of the initially cuboidal  $\gamma'$  precipitates [53]—has occurred (Fig. 8 C3).  $\gamma'$  coalescence in the horizontal direction is another indication of negative lattice misfit at creep temperature:  $\gamma'$  has a smaller lattice parameter compared to  $\gamma$  [4,13].

An increase in the applied tensile stress reduces the volume fraction of the dislocation-depleted regions. At section E, no dislocation-depleted region remains. Fig. 8 E1 depicts a low angle boundary and its adjoining crystals avalanched by dislocations at  $\gamma/\gamma'$  interfaces. Fig. 8 E2-TS and its magnified counterpart in Fig. 8 E3-TS display a region far from any boundary. These regions are not different from the regions in the vicinity of a low-angle boundary. Rafting has occurred in both regions. The dislocation density in boundary-free regions (Fig. 7 b) amounts to  $10^{14} \text{ m}^{-2}$ . At section D, the microstructure does not differ from that in section E.

As stated before, at section B, there is no dislocation-avalanched region; and at section D, there is no dislocation-depleted region. We appoint the point where the first dislocation-avalanched region is observed as where the creep deformation commences. In the testpiece examined here, it is located at 3.1 mm before the gauge root, which is after section B and just before section C. Any region before this point—including the region that was termed “the uncrept region” in §3.1—is considered as undeformed here.

cECCI-based dislocation characterization on {001} cross-sections (e.g. Fig. 8 E2-TS magnified in Fig. 8 E3-TS) shows that the avalanche dislocation at the horizontal (001)  $\gamma/\gamma'$  interfaces with a  $1/2\langle 110 \rangle$  Burgers vector and a  $\langle 110 \rangle$  line direction, which make a  $45^\circ$  angle to the {100} habit planes of the  $\gamma'$  cubes, are predominantly  $60^\circ$  mixed [10,54,55]. An example of dislocation characterization is presented in supplementary material S2.

### 3.3. Modelling of possible creep dislocation sources

The aim of employing DDD modelling here is to examine the possible sources of the experimentally observed avalanche creep dislocations. Based on the ECCI observations of the uncrept region, two initial dislocation microstructures were considered as starting microstructures for DDD simulations: (1) a dislocation arrangement constituting a grown-in low-angle boundary (Fig. 9 a) and (2) a set of individual dislocations spread in a boundary-free region (Fig. 9 e).

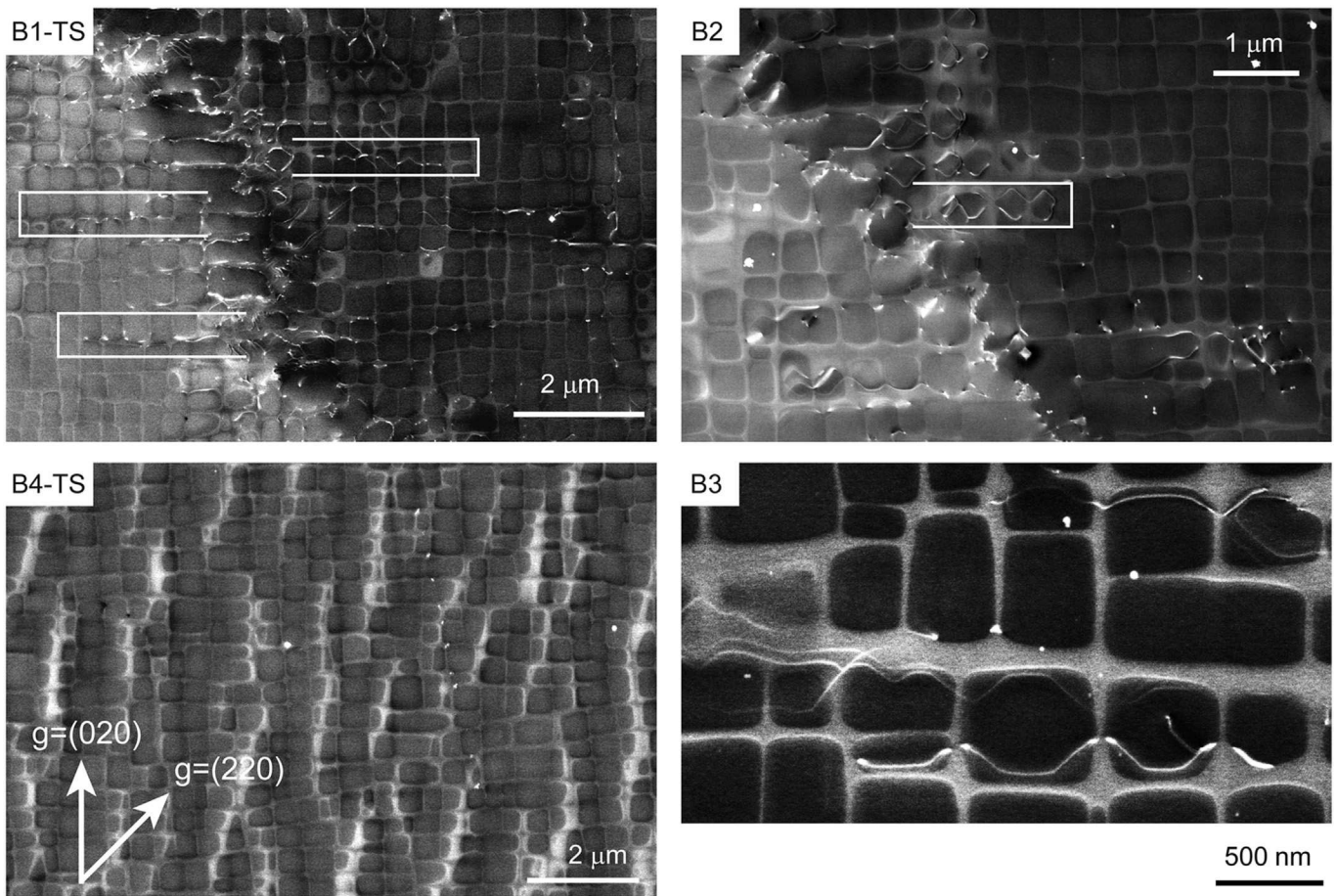


Fig. 8. (continued).

For both simulations, the simulation cell was a cube of  $1.5 \mu\text{m}$  edge length, which included  $3 \times 3 \times 3$  cuboidal  $\gamma'$  particles with a  $0.42 \mu\text{m}$  side length separated by  $0.08 \mu\text{m}$ -wide  $\gamma$  channels; Periodic boundary conditions (PBC) were applied along the three cubic axes of the simulation cell; and a uniaxial stress of 450 MPa was applied along the  $[001]$  crystallographic direction.

The first simulation set-up consisted of 10 mixed  $\frac{1}{2}[011]$  dislocations, which comprised a low-angle boundary with a  $[010]$  normal (Fig. 9 a). In accord with the HR-EBSD- and cECI-based studies presented in §3.1, the density of the mobile dislocations arranged in form of the low angle boundary was assumed to be  $6 \times 10^{12} \text{m}^{-2}$ .

The results of this simulation show that as creep deformation proceeds, a planar dislocation front originates at the low-angle boundary and moves away from it (Fig. 9 b). The dislocation front is better visible when the simulation cell is viewed along the tensile axis (Fig. 9 c). The speed of the dislocation front is  $\sim 1.5 \mu\text{m}$  per 0.1% creep deformation. This approximation is made by examining the simulation cell at 0.07% plastic strain, where the interaction of the percolating dislocations with the next low-angle boundary, which is located  $1.5 \mu\text{m}$  away, is negligible. At 0.14% creep strain, all dislocations reach the opposite side of the simulation cell, which is  $1.5 \mu\text{m}$  away from its origin. At this point, the simulation cell is homogeneously saturated with dislocations (Fig. 9 d). Dislocation density and rate of dislocation multiplication ( $\partial\rho_d/\partial\varepsilon_p$ ) as a function of plastic strain are plotted in Fig. 10. As the red curve in this plot shows, at 0.1% plastic strain, dislocation density reaches  $8 \times 10^{13} \text{m}^{-2}$ , which is almost 13 times the initial dislocation

density.

A brief description of the simulation results is presented in the following. Under the applied stress, dislocations are mobilized in the vertical channel and then are immediately locked on the vertical  $\gamma/\gamma'$  interfaces. The dislocation segments located between the particles are able to bow out into the  $\gamma$  channels crossing the initial vertical channel and thus to deposit dislocation dipoles along the  $\langle 110 \rangle$  directions. This results in a notable dislocation multiplication rate at the onset of creep, which gives rise to the initial large peak seen in the  $\partial\rho_d/\partial\varepsilon_p$  curve in Fig. 10. Those segments then propagate further within all the channels with combined glide-climb mobility (Fig. 9 b and c), where short-range interactions between dislocations notably reduces the rate of multiplication. By further percolation of dislocations through the  $\gamma/\gamma'$  microstructure, dislocation density increases; however, the rate of multiplication and its contribution to plastic strain decreases. This reduction in dislocation generation rate is indicated by the in Fig. 10. At 0.07% plastic strain, marked by arrow (1), the proceeding dislocation segments approach the next low-angle boundary located  $1.5 \mu\text{m}$  away (Fig. 9 b and c), where, due to dislocation–dislocation interactions, further progress of the dislocations is nontrivial. At 0.14% plastic strain, shown by arrow (2), the simulation cell of  $3.4 \mu\text{m}^3$  volume is homogeneously saturated with dislocations as appears in Fig. 9 d. Both of these stages are followed by a drop in dislocation multiplication rate. When the microstructure is homogeneously saturated with dislocations, the dislocation multiplication rate decreases dramatically; and subsequently, the glide-climb mobility of dislocations plays the prominent role in the accumulation of

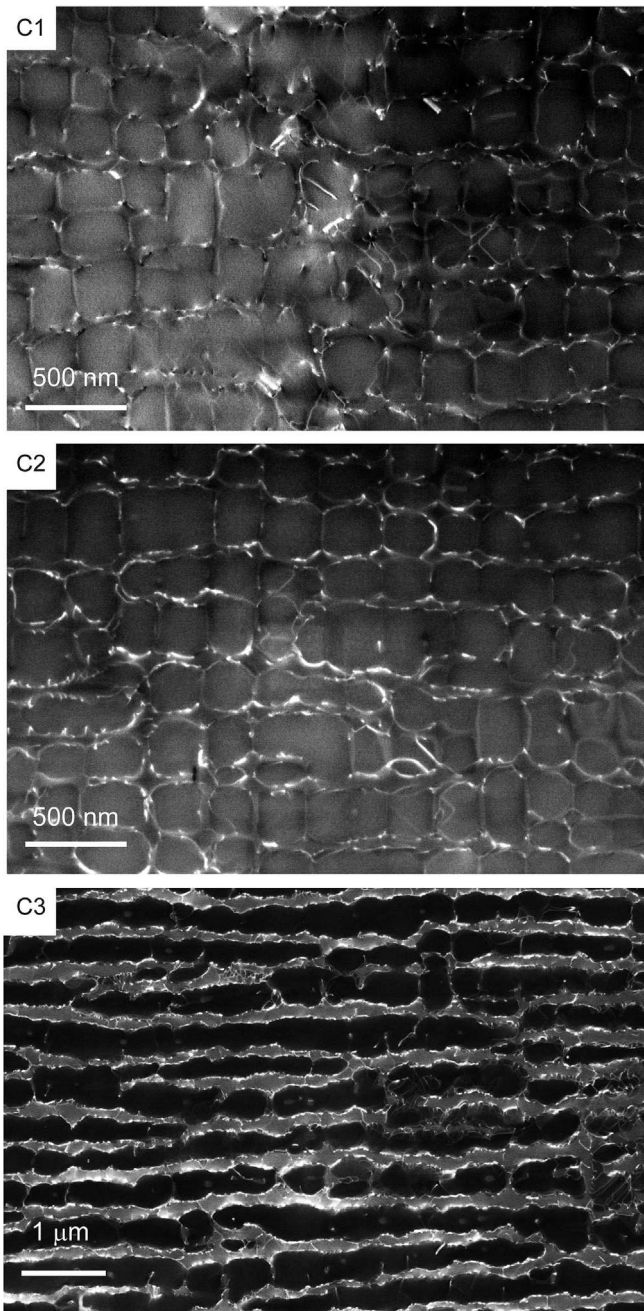


Fig. 8. (continued).

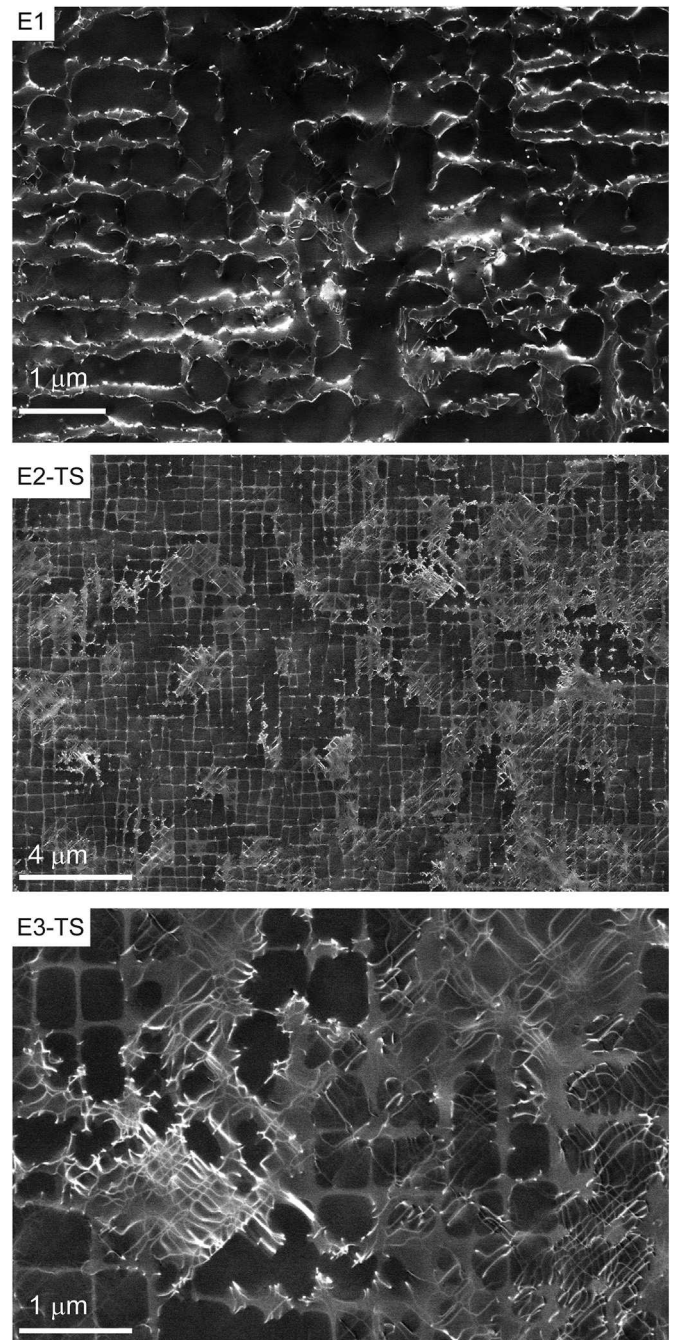


Fig. 8. (continued).

plastic strain [30].

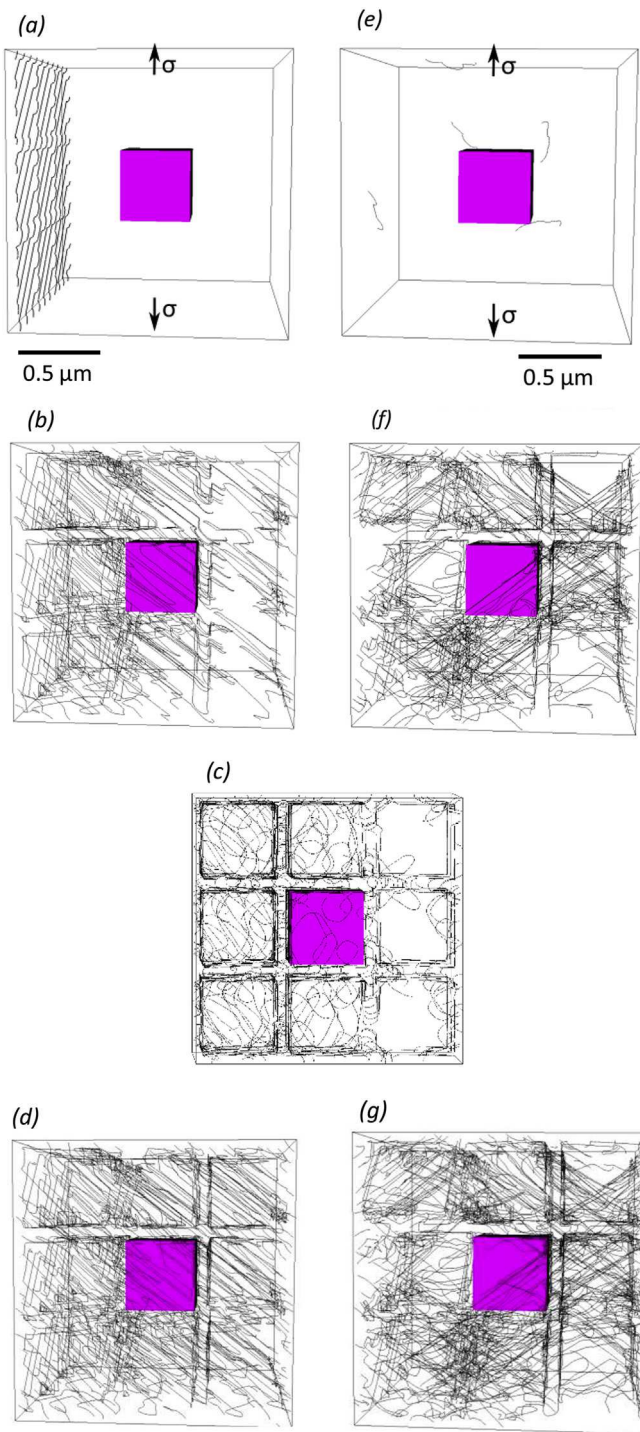
The second simulation set-up consisted of five Frank-Read (FR) sources of  $\frac{1}{2} \langle 011 \rangle$  mixed character with a line length of  $0.35 \mu\text{m}$  (Fig. 9 e). The starting dislocation density was taken to be  $5 \times 10^{11} \text{ m}^{-2}$ , which represents the low populated regions away from low-angle boundaries in the uncrept region (e.g. Fig. 8 A3). The evolution of the dislocation microstructure due to an applied uniaxial stress of 450 MPa along the [001] direction is shown in Fig. 9 e–g. Fig. 9 e shows the bowing FR sources at an early deformation stage, which leads to the propagation of the sources along different {011} glide planes in Fig. 9 f. After a slight deformation, the microstructure mainly consists of dislocation lines parallel to the  $\langle 110 \rangle$  directions, which are deposited on the  $\gamma/\gamma'$  interfaces (Fig. 9 g). The green curve in Fig. 10 shows the variation of

Table 1

The character of the dislocations in the uncrept region of the ruptured testpiece. In total, 155 dislocations over 27 boundaries were characterized by controlled electron channeling contrast imaging (cECCI).

Character	Screw	60° mixed	Edge		
Burgers vector	$\frac{1}{2} \langle 011 \rangle$			$\langle 100 \rangle$	
Slide plane	{111}			Sessile	
%	7.8	40	30.3	16.1	5.8

dislocation density ( $\rho_d$ ) as a function of plastic strain ( $\epsilon_p$ ) for this simulation. At  $\sim 0.1\%$  plastic strain, dislocation density reaches  $8 \times 10^{13} \text{ m}^{-2}$ , which is more than two orders of magnitude higher



**Fig. 9.** DDD simulations.—(a–d) Percolation of the  $\frac{1}{2}$  [011] mixed dislocation arrangements constituting a low-angle (010) boundary of  $0.6 \times 10^{13} \text{ m}^{-2}$  dislocation density at (a) 0.0%, (b and c) 0.08%, and (d) 0.14% plastic strain. (e–g) Percolation of the individual  $\frac{1}{2}$  <011> Frank-Read (FR) sources of  $5 \times 10^{11} \text{ m}^{-2}$  starting dislocation density at (e) 0.0%, (f) 0.12%, and (g) 0.18% plastic strain. Simulations are carried out at 450 MPa tensile stress applied along the [001] direction with a climb/glide mobility ratio of 0.1. The tensile axis in all but (c) is directed as shown in (a). In (c) the simulation cell is viewed along the tensile axis. For clarity, only one  $\gamma'$  particle is shown in each simulation cell.

than the density before deformation:  $5 \times 10^{11} \text{ m}^{-2}$ .

At  $\sim 0.1\%$ , the increase in dislocation content is significantly higher in boundary-free regions compared to the vicinity of

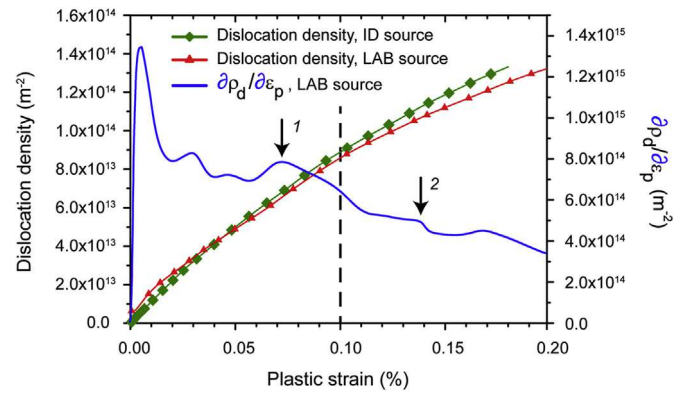


**Fig. 10.** Dislocation density ( $\rho_d$ ) and rate of dislocation multiplication ( $\partial\rho_d/\partial\epsilon_p$ ) as a function of plastic strain ( $\epsilon_p$ ) due to the percolation of dislocations through the  $\gamma/\gamma'$  microstructure. The two cases shown in Figure 9—i.e. dislocations originated at a low-angle, grown-in boundary (LAB) source and dislocations generated by individual dislocation (ID) sources through the Frank-Read mechanism—are plotted.

boundaries—two orders of magnitude versus 13 times. This difference is due to the different mechanisms of dislocation creep in the two regions. The simulations show that while the glide-climb mobility along the  $\gamma/\gamma'$  interfaces is the dominant mechanism in the vicinity of low-angle boundaries, the glide of propagating dislocations along  $\gamma$  channels is the governing mechanism in boundary-free regions.

#### 4. Discussion

This work was aimed at investigating the origin of creep dislocations. Based on ECCI observations, it was shown that at the very early stages of creep, when creep strain is below 0.1%, creep dislocations avalanche the entire microstructure. Due to this avalanche, dislocation density in initially dislocation-depleted regions soars by two orders of magnitude. The widely accepted hypothesis in superalloy literature is that creep dislocations are originated at grown-in, low-angle boundaries [11,13,14,56]. The present work, in contrast, shows that boundaries are neither the exclusive nor the main sources of creep dislocations: they only account for a small fraction of creep dislocations.

Studies that attributed creep dislocations to low-angle boundaries did so by observing dislocation loop segments originating from low-angle boundaries and percolating through dislocation-depleted crystals at the very early stages of creep. These dislocation loop segments were also observed here (Fig. 8 B1-TS, B2, and B3). Nevertheless, never was a boundary-originated dislocation observed to percolate more than a few  $\gamma$  channels away from a boundary into the adjoining crystal. Neither among the TEM-based studies is there a record of such observation [11,13,56]. This lack of evidence suggests that the boundary-originated dislocations remain close to the boundary. This suggestion was here confirmed by the results of the DDD simulation of boundary-originated dislocations (Fig. 9 a–d and Fig. 10), which showed that although at 0.1% creep strain,  $\sim 10^{14} \text{ m}^{-2}$  dislocations are generated by a low-angle boundary, the percolation rate of the generated dislocations is so small—1.5  $\mu\text{m}$  per 0.1% of creep strain—that they remain confined to the close vicinity of their source boundary.

By combining the results of the experimental observations and modelling, it can be concluded that: low-angle boundaries account for only a minor portion of creep dislocations—those that appear in their close vicinity. Note that low-angle boundaries are on average 60  $\mu\text{m}$  apart; boundary-originated dislocations cover only a few micrometers of this distance. Creep dislocations that deluge the

microstructure away from boundaries must have sources other than low-angle boundaries. This conclusion is supported by reports on the anteriority of plastic deformation and rafting in dendritic cores to the same in interdendritic regions at the very early stages of creep [54,55], which give an indication of different deformation mechanisms in the vicinity and away from boundaries.

Possible sources of avalanching dislocations are the individual dislocations that are spread in boundary-free regions in small quantities ( $5 \times 10^{11} \text{ m}^{-2}$ ), such as the dislocations marked by arrows in Fig. 8 A3 and Fig. 8 B4. These, if pinned, can emit dislocations by Frank-Read [57] or double cross-slip [58] mechanisms when their critical resolved shear stress is reached.

We could not examine this hypothesis experimentally; thus, DDD modelling was employed for this purpose. The simulation results showed that despite their much smaller initial density compared to the initial density of dislocations at low-angle boundaries, at  $\sim 0.1\%$  strain, individual dislocations can fill the boundary-free microstructure with  $\sim 10^{14} \text{ m}^{-2}$  creep dislocations. They are able to propagate along different directions with less interaction with nearby dislocations in comparison to those emitted from the grown-in, low-angle boundaries. This promotes their percolation rate. Moreover, as they are spatially homogeneously distributed, so are the dislocations they generate. Thus, they can create dislocation avalanches analogous to those observed in the ECCI micrographs of the boundary-free regions at early stages of creep.

In summary, in this work, it was shown that at the early stages of creep, grown-in, low-angle boundaries are only the sources of dislocations that appear in their close vicinity. Sources of creep dislocations that emerge anywhere else in the microstructure are the isolated, individual dislocations, which are uniformly dispersed in the undeformed microstructure with a small  $\sim 5 \times 10^{11} \text{ m}^{-2}$  population.

## 5. Conclusions

- 1) There is an intricate network of low-angle boundaries in an undeformed single-crystal superalloy. The boundary spacing is 30–150  $\mu\text{m}$ ; misorientation across these boundaries is below  $0.5^\circ$ ; and the density of geometrically necessary dislocations at these boundaries does not exceed  $5 \times 10^{13} \text{ m}^{-2}$ .
- 2) Grown-in, low-angle boundaries are neither the exclusive nor the major sources of creep dislocations at the early stages of creep. At a creep strain below 0.1%, dislocation density in the entire microstructure soars by two orders of magnitude—from  $5 \times 10^{11} \text{ m}^{-2}$  in the undeformed state to  $10^{14} \text{ m}^{-2}$  in the lightly-crept state. Low-angle boundaries account for only a small fraction of creep dislocations: those that appear in their close vicinity. They are, however, not the sources of dislocations that emerge in regions farther than a few  $\gamma$  channels away from any boundary. These dislocations are generated by isolated, individual dislocations dispersed in boundary-free regions of the uncrept material.

## Acknowledgements

RR would like to thank Alexander von Humboldt Foundation's financial support, which he has received through the Humboldt Research Award.

## Appendix A. Supplementary data

Supplementary data related to this article can be found at <http://dx.doi.org/10.1016/j.actamat.2016.02.038>.

## References

- [1] J.D. Miller, T.M. Pollock, Stability of dendrite growth during directional solidification in the presence of a non-axial thermal field, *Acta Mater.* 78 (2014) 23–36.
- [2] C. Panwisawas, H. Mathur, J.-C. Gebelin, D. Putman, C.M.F. Rae, R.C. Reed, Prediction of recrystallization in investment cast single-crystal superalloys, *Acta Mater.* 61 (2013) 51–66.
- [3] J.S. Van Sluytman, T.M. Pollock, Optimal precipitate shapes in nickel-base  $\gamma$ - $\gamma'$  alloys, *Acta Mater.* 60 (2012) 1771–1783.
- [4] R.C. Reed, *The Superalloys, Fundamentals and Applications*, in: *The Superalloys*, 2006 (p. various).
- [5] E.M. Francis, B.M.B. Grant, J.Q. da Fonseca, P.J. Phillips, M.J. Mills, M.R. Daymond, et al., High-temperature deformation mechanisms in a polycrystalline nickel-base superalloy studied by neutron diffraction and electron microscopy, *Acta Mater.* 74 (2014) 18–29.
- [6] G.B. Viswanathan, R. Shi, A. Genc, V.A. Vorontsov, L. Kovarik, C.M.F. Rae, et al., Segregation at stacking faults within the  $\gamma'$  phase of two Ni-base superalloys following intermediate temperature creep, *Scr. Mater.* 94 (2015) 5–8.
- [7] V.A. Vorontsov, L. Kovarik, M.J. Mills, C.M.F. Rae, High-resolution electron microscopy of dislocation ribbons in a CMSX-4 superalloy single crystal, *Acta Mater.* 60 (2012) 4866–4878.
- [8] P.M. Sarosi, R. Srinivasan, G.F. Eggeler, M.V. Nathal, M.J. Mills, Observations of  $a(010)$  dislocations during the high-temperature creep of Ni-based superalloy single crystals deformed along the  $[001]$  orientation, *Acta Mater.* 55 (2007) 2509–2518.
- [9] C.M.F. Rae, R.C. Reed, Primary creep in single crystal superalloys: Origins, mechanisms and effects, *Acta Mater.* 55 (2007) 1067–1081.
- [10] V. Sass, M. Feller-Kniepmeier, Orientation dependence of dislocation structures and deformation mechanisms in creep deformed CMSX-4 single crystals, *Mater. Sci. Eng. A* 245 (1998) 19–28.
- [11] T.M. Pollock, A.S. Argon, Creep resistance of CMSX-3 nickel base superalloy single crystals, *Acta Metall. Mater.* 40 (1992) 1–30.
- [12] T.M. Pollock, A.S. Argon, Directional coarsening in nickel-base single crystals with high volume fractions of coherent precipitates, *Acta Metall. Mater.* 42 (1994) 1859–1874.
- [13] T.M. Pollock, R.D. Field, Chapter 63 Dislocations and High-Temperature Plastic Deformation of Superalloy Single Crystals, 2002, pp. 547–618.
- [14] T. Link, A. Epishin, B. Fedelich, Inhomogeneity of misfit stresses in nickel-base superalloys: effect on propagation of matrix dislocation loops, *Philos. Mag.* 89 (2009) 1141–1159.
- [15] N. Siredey, M. Boufoussi, S. Denis, J. Lacaze, Dendritic growth and crystalline quality of nickel-base single grains, *J. Cryst. Growth* 130 (1993) 132–146.
- [16] C. Lang, W. Schneider, H. Mughrabi, X-ray investigations on creep-deformed single crystals of the nickel-base superalloy CMSX-4, *Acta Metall. Mater.* 43 (1995) 1751–1764.
- [17] N.S. Hussein, D.P. Kumah, J.Z. Yi, C.J. Torbet, D.A. Arms, E.M. Dufresne, et al., Mapping single-crystal dendritic microstructure and defects in nickel-base superalloys with synchrotron radiation, *Acta Mater.* 56 (2008) 4715–4723.
- [18] U. Brückner, A. Epishin, T. Link, Local X-ray diffraction analysis of the structure of dendrites in single-crystal nickel-base superalloys, *Acta Mater.* 45 (1997) 5223–5231.
- [19] A. Epishin, T. Link, G. Nolze, SEM investigation of interfacial dislocations in nickel-base superalloys, *J. Microsc.* 228 (2007) 110–117.
- [20] A.K. Singh, N. Louat, K. Sadananda, Dislocation network formation and coherency loss around gamma-prime precipitates in a nickel-base superalloy, *Metall. Trans. A Phys. Metall. Mater. Sci.* 19 A (1988) 2965–2973.
- [21] R.C. Reed, T. Tao, N. Warnken, Alloys-by-design: application to nickel-based single crystal superalloys, *Acta Mater.* 57 (2009) 5898–5913.
- [22] I. Gutierrez-Urrutia, S. Zaefferer, D. Raabe, Coupling of electron channeling with EBSD: toward the quantitative characterization of deformation structures in the SEM, *JOM* 65 (2013) 1229–1236.
- [23] S. Zaefferer, N.-N. Elhami, Theory and application of electron channelling contrast imaging under controlled diffraction conditions, *Acta Mater.* 75 (2014) 20–50.
- [24] M.A. Crimp, Scanning electron microscopy imaging of dislocations in bulk materials, using electron channeling contrast, *Microsc. Res. Tech.* 69 (2006) 374–381.
- [25] A.J. Schwartz, M. Kumar, B.L. Adams, D.P. Field (Eds.), *Electron Backscatter Diffraction in Materials Science*, Springer US, Boston, MA, 2009.
- [26] S. Zaefferer, New developments of computer-aided crystallographic analysis in transmission electron microscopy, *J. Appl. Crystallogr.* 33 (2000) 10–25.
- [27] S. Zaefferer, Computer-aided crystallographic analysis in the TEM, in: *Adv. Imaging Electron Phys.* 2003, 355–XII.
- [28] A.J. Schwartz, M. Kumar, B.L. Adams (Eds.), *Electron Backscatter Diffraction in Materials Science*, Springer US, Boston, MA, 2000, <http://dx.doi.org/10.1007/978-1-4757-3205-4>.
- [29] N.C. Krieger Lassen, Automatic localisation of electron backscattering pattern bands from Hough transform, *Mater. Sci. Technol.* 12 (1996) 837–843.
- [30] A.J. Wilkinson, G. Meaden, D.J. Dingley, High-resolution elastic strain measurement from electron backscatter diffraction patterns: new levels of sensitivity, *Ultramicroscopy* 106 (2006) 307–313.
- [31] A.J. Wilkinson, G. Meaden, D.J. Dingley, High resolution mapping of strains and rotations using electron backscatter diffraction, *Mater. Sci. Technol.* 22

- (2006) 1271–1278.
- [32] A.J. Wilkinson, D. Randman, Determination of elastic strain fields and geometrically necessary dislocation distributions near nanoindentations using electron back scatter diffraction, *Philos. Mag.* 90 (2010) 1159–1177.
- [33] J. Jiang, T.B. Britton, A.J. Wilkinson, Evolution of dislocation density distributions in copper during tensile deformation, *Acta Mater.* 61 (19) (2013) 7227–7239, <http://dx.doi.org/10.1016/j.actamat.2013.08.027>.
- [34] J.F. Nye, Some geometrical relations in dislocated crystals, *Acta Metall.* 1 (1953) 153–162, [http://dx.doi.org/10.1016/0001-6160\(53\)90054-6](http://dx.doi.org/10.1016/0001-6160(53)90054-6).
- [35] X. Zhang, P.R. Stoddart, J.D. Comins, A.G. Every, High-temperature elastic properties of a nickel-based superalloy studied by surface Brillouin scattering, *J. Phys. Condens. Matter* 13 (2001) 2281–2294.
- [36] T.B. Britton, A.J. Wilkinson, Measurement of residual elastic strain and lattice rotations with high resolution electron backscatter diffraction, *Ultramicroscopy* 111 (2011) 1395–1404.
- [37] S.M. Keralavarma, T. Cagin, A. Arsenlis, A.A. Benzerga, Power-law creep from discrete dislocation dynamics, *Phys. Rev. Lett.* 109 (2012).
- [38] S.M. Hafez Haghighat, G. Eggeler, D. Raabe, Effect of climb on dislocation mechanisms and creep rates in  $\gamma'$ -strengthened Ni base superalloy single crystals: a discrete dislocation dynamics study, *Acta Mater.* 61 (2013) 3709–3723.
- [39] K. Danas, V.S. Deshpande, Plane-strain discrete dislocation plasticity with climb-assisted glide motion of dislocations, *Model. Simul. Mater. Sci. Eng.* 21 (2013) 045008.
- [40] C. Ayas, J.A.W. Van Dommelen, V.S. Deshpande, Climb-enabled discrete dislocation plasticity, *J. Mech. Phys. Solids* 62 (2014) 113–136.
- [41] D. Raabe, Introduction of a hybrid model for the discrete 3D simulation of dislocation dynamics, *Comput. Mater. Sci.* 11 (1998) 1–15.
- [42] B. Liu, D. Raabe, F. Roters, A. Arsenlis, Interfacial dislocation motion and interactions in single-crystal superalloys, *Acta Mater.* 79 (2014) 216–233.
- [43] B. Liu, P. Eisenlohr, F. Roters, D. Raabe, Simulation of dislocation penetration through a general low-angle grain boundary, *Acta Mater.* 60 (2012) 5380–5390.
- [44] A. Arsenlis, W. Cai, M. Tang, M. Rhee, T. Opperstrup, G. Hommes, et al., Enabling strain hardening simulations with dislocation dynamics, *Model. Simul. Mater. Sci. Eng.* 15 (2007) 553–595.
- [45] A.B. Parsa, P. Wollgramm, H. Buck, C. Somsen, A. Kostka, I. Povstugar, et al., Advanced scale bridging microstructure analysis of single crystal Ni-base superalloys, *Adv. Eng. Mater.* 17 (2015) 216–230, <http://dx.doi.org/10.1002/adem.201400136>.
- [46] S.I. Wright, M.M. Nowell, R. de Kloe, L. Chan, Orientation precision of electron backscatter diffraction measurements near grain boundaries, *Microsc. Microanal.* (2014) 1–12, <http://dx.doi.org/10.1017/S143192761400035X>.
- [47] F. Ram, S. Zaeferrer, T. Jäpel, D. Raabe, Error analysis of the crystal orientations and disorientations obtained by the classical electron backscatter diffraction technique, *J. Appl. Crystallogr.* 48 (2015) 797–813, <http://dx.doi.org/10.1107/S1600576715005762>.
- [48] S.I. Wright, M.M. Nowell, D.P. Field, A review of strain analysis using electron backscatter diffraction, *Microsc. Microanal.* 17 (2011) 316–329.
- [49] D.P. Field, C.C. Merriman, N. Allain-Bonasso, F. Wagner, Quantification of dislocation structure heterogeneity in deformed polycrystals by EBSD, *Model. Simul. Mater. Sci. Eng.* 20 (2012) 24007.
- [50] J. Jiang, T.B. Britton, A.J. Wilkinson, Measurement of geometrically necessary dislocation density with high resolution electron backscatter diffraction: effects of detector binning and step size, *Ultramicroscopy* 125 (2013) 1–9, <http://dx.doi.org/10.1016/j.ultramic.2012.11.003>.
- [51] H. Gabrisch, D. Mukherji, R.P. Wahi, Deformation-induced dislocation networks at the  $\gamma$ - $\gamma'$  interfaces in the single-crystal superalloy SC16: A mechanism-based analysis, *Philos. Mag. A* 74 (1996) 229–249.
- [52] E. Underwood, in: J.L. McCall, W.M. Mueller (Eds.), *Microstructural Analysis*, Springer US, Boston, MA, 1973, pp. 35–66, <http://dx.doi.org/10.1007/978-1-4615-8693-7>.
- [53] F.R.N. Nabarro, Rafting in superalloys, *Metall. Mater. Trans. A* 27 (1996) 513–530.
- [54] M. Kolbe, A. Dlouhy, G. Eggeler, Dislocation reactions at  $\gamma/\gamma'$ -interfaces during shear creep deformation in the macroscopic crystallographic shear system (001)[110] of CMSX6 superalloy single crystals at 1025°C, *Mater. Sci. Eng. A* 246 (1998) 133–142, [http://dx.doi.org/10.1016/S0921-5093\(97\)00733-8](http://dx.doi.org/10.1016/S0921-5093(97)00733-8).
- [55] J.Y. Buffiere, M. Ignat, A dislocation based criterion for the raft formation in nickel-based superalloys single crystals, *Acta Metall.* 43 (1995) 1791–1797, [http://dx.doi.org/10.1016/0956-7151\(94\)00432-H](http://dx.doi.org/10.1016/0956-7151(94)00432-H).
- [56] J. Zhang, J. Wang, H. Harada, Y. Koizumi, The effect of lattice misfit on the dislocation motion in superalloys during high-temperature low-stress creep, *Acta Mater.* 53 (2005) 4623–4633.
- [57] F.C. Frank, W.T. Read, Multiplication processes for slow moving dislocations, *Phys. Rev.* 79 (1950) 722–723.
- [58] J.S. Koehler, The nature of work-hardening, *Phys. Rev.* 86 (1952) 52–59.